
Article:
Koc, M., Wang, J. and Sun, T. (2016) An Inverter Nonlinearity Independent Flux Observer for Direct Torque Controlled High Performance Interior Permanent Magnet Brushless AC Drives. IEEE Transactions on Power Electronics. ISSN 0885-8993

https://doi.org/10.1109/TPEL.2016.2524644

An Inverter Nonlinearity Independent Flux Observer for Direct Torque Controlled High Performance Interior Permanent Magnet Brushless AC Drives

Mikail Koç, Student Member, IEEE, Jiabin Wang, Senior Member, IEEE, Tianfu Sun, Student Member, IEEE

Abstract—This paper introduces a novel flux observer for direct torque controlled (DTC) interior permanent magnet brushless AC (IPM-BLAC) drives over a wide speed range including standstill. The observer takes machine nonlinearities into account and is independent of inverter nonlinearities, dead-time and armature resistance variation at steady-states since such inaccuracies are compensated quickly by measured phase currents. Magnetic saturations in the stator and rotor cores, cross-coupling effects of flux linkages of the motor and spatial harmonics in the magneto-motive force (MMF) are all considered in the novel scheme. There is no filter; hence no delays and oscillatory responses like in conventional schemes where filters are employed to prevent integrator drift issue. Superiority of the observer when compared to the state-of-the-art schemes has been illustrated by both extensive simulations and experimental results of a 10kW IPM-BLAC machine designed for traction applications.

Index Terms—Direct Torque Control, Flux Observer, High Performance Drives, Nonlinear Inverter, IPMSM

I. INTRODUCTION

TRANSPORTATION industry is moving from internal combustion based vehicles to eco-friendly electric vehicles (EVs) since they can use renewable and sustainable energy technologies.

IPM-BLAC machines are widely and increasingly used in EVs due to their superior characteristics such as high efficiency, low noise, low rotor losses, robustness due to buried magnets, high field weakening (FW) capability over a wide speed range, and highest torque to power ratio of all machines due to high saliency and reluctance torque [1-3].

In modern electric drives, control of AC machines can be classified into 2 categories based on the rotating control frames which are rotor (dq) and stator flux ($f\tau$ - Fig. 1) frames [4]. dq and $f\tau$ frames rotate in synchronism with the rotor angle, θ_e, and the stator flux angle, $\theta_f = \theta_e + \delta$, respectively. The controls in dq and $f\tau$ frames are generally defined as field oriented control (FOC) and direct torque control (DTC), respectively.

The basic difference between FOC and DTC is the way of torque control. It is controlled indirectly through dq-axis currents in FOC, but is controlled directly in DTC drives. Thus, instead of currents, which can be measured, torque and stator flux magnitude, which needs to be observed, are required in DTC drives. Because torque is a function of stator flux vector [4], it is necessary and sufficient to observe the flux vector with an acceptable accuracy. Hence, flux observer quality is of paramount importance in DTC drives.

To date, a wide range of flux observers have been researched in the literature and employed in drives [5-13]. These can be classified in three main categories, viz., current model (CM) based, voltage model (VM) based and hybrid model (HM) closed loop flux observers.

A VM based observer is robust to machine parameter variations and nonlinearities at high speeds except the armature resistance variation but it is vulnerable to measurement errors at low speeds. When motor speed is low, where the voltages and electrical frequency are very low, the flux estimation is greatly influenced by inverter nonlinearity and not accurate. Accordingly, the drive might fail since the flux information in the controller may differ significantly from the actual one. In fact, machines cannot start properly with this estimation method [10, 11, 14-16]. In such cases machine operation has been investigated either above a certain speed or the observer has been manually switched from CM to VM mode. These observers are also remarkably sensitive to inverter nonlinearities, dead-time, and armature resistance variation even at high speeds unless they are compensated. Further, as VM based observers are vulnerable to pure integration due to drift issue, generally LPFs are employed to handle the issue [9, 11, 17-19] resulting in delayed and oscillatory response as the filtered outputs require necessary phase and magnitude compensations.

A CM based observer, on the other hand, is robust to measurement error at low speeds; however, this method is vulnerable to machine parameter variations and nonlinearities which is an important drawback for high performance IPM-BLAC drives whose parameters may change significantly. In a practical application, magnetic saturation, temperature,

Manuscript received September 23, 2015; revised December 10, 2015; accepted January 25, 2016.

The authors are with the department of electronic and electrical engineering, The University of Sheffield, Mappin Street, Sheffield S1 3JD, United Kingdom (e-mail: mikaelkoc@gmail.com, j.b.wang@sheffield.ac.uk, tianfu.sun@foxmail.com).

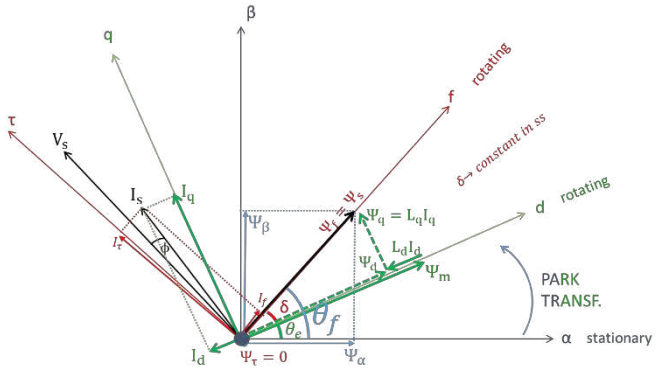

Fig. 1 Stationary ($\alpha\beta$), rotor (dq) and stator flux ($f\tau$) reference frames

manufacture tolerance, cross-coupling, and variations on the material properties might greatly contribute to deviations of the parameters [20] and machine nonlinearities from those used in the CM based observer.

Considering merits of CM and VM methods, an HM observer has been developed in [5] and improved in [8]. The HM observer structure has been commonly used in the literature in recent years for not only IPM-BLAC machines [13, 21-23] but other machine types [8, 18] as well. Therefore, a large number of state-of-the-art DTC drives utilize CM and VM based observers at low and high speeds, respectively.

The HM based observer structure, however, still has the drawbacks of CM and VM based observers at low and high speeds, respectively, and introduces performance deterioration during transitions from CM to VM or vice-versa. The flux transition trajectory is illustrated in Fig. 2-a. Attempts are made in [8] to linearize the trajectory for induction machines as illustrated in Fig. 2-b. Indeed, performance deterioration still exists during flux transitions and linearization implementation is complicated. More importantly, inaccuracies of flux estimation in the VM mode degrade the accuracy of the HM based observer even at low speeds and vice-versa. Because the VM based observer accuracy becomes extremely poor when the speed approaches to zero, the performance and current waveforms of the drive with the HM observer significantly deteriorate.

Estimation inaccuracies of an HM based observer might be high at low speeds, depending on the level of magnetic saturation. To handle this, [9] proposed a modified HM observer for FOC drives in order to improve current controller performance. The modified observer is robust to parameter variations at low speeds but its performance deteriorates when speed approaches to zero. Further, it is difficult to balance the trade-off between the controller and observer bandwidths for optimal performance. Recently, the work reported in [6] proposed a disturbance input decoupling observer structure for a DTC drive similar to that in [9]. The proposed technique aims to achieve robust estimation even at zero speed. However, the use of high pass and low pass filters not only increases the complexity, but introduces inevitable time delay.

Ultimately, observer inaccuracies will affect flux and torque control quality and hence, the drive efficiency. To address this problem, a novel flux observer for direct torque controlled IPM-BLAC drives is proposed in this paper. The proposed observer accounts for:

- magnetic saturation in the stator and rotor cores,
- cross-coupling effects of dq-axis flux linkages,
- spatial harmonics in the magneto-motive force (MMF),

and is robust against:

- armature resistance variation with temperature,
- the voltage drop on the inverter output,
- dead-time.

Moreover, it avoids torque-flux oscillations due to filters and performance deterioration during speed transition and at low speeds of the conventional schemes. Hence, the IPM drives with the proposed observer has high performance over a wide speed range.

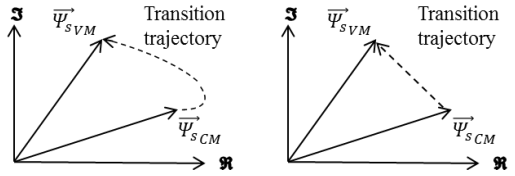

(a) conventional (b) proposed in [8]

Fig. 2 Transition trajectories of HM observers from CM to VM mode

II. Direct Torque Control

A. Modelling of IPM BLAC Machines

Clark and Park transformations of 3-axis stationary ABC frame equations give 2-axis rotating reference frame equations of AC machines. Rotor (dq) and stator flux ($f\tau$) frame modelling of machines are obtained when the rotor angle (θ_e) and the stator flux angle ($\theta_f = \theta_e + \delta$) are used in Park transformations, respectively (Fig. 1). The well-known peak convention modelling of IPM-BLAC machines in rotor frame are given as follows [4]:

$$\begin{bmatrix} V_d \\ V_q \end{bmatrix} = R \begin{bmatrix} I_d \\ I_q \end{bmatrix} + \frac{d}{dt} \begin{bmatrix} \Psi_d \\ \Psi_q \end{bmatrix} + w \begin{bmatrix} -\Psi_q \\ \Psi_d \end{bmatrix} \quad (1)$$

$$\begin{bmatrix} \Psi_d \\ \Psi_q \end{bmatrix} = \begin{bmatrix} L_d & 0 \\ 0 & L_q \end{bmatrix} \begin{bmatrix} I_d \\ I_q \end{bmatrix} + \begin{bmatrix} \Psi_m \\ 0 \end{bmatrix} \quad (2)$$

$$T_e = \frac{3p}{2} \left[\Psi_d I_q - \Psi_q I_d \right] \quad (3)$$

where I_{dq}, V_{dq}, Ψ_{dq} are the rotor frame currents, voltages and flux linkages, respectively. Ψ_m is the magnetic flux linkage, p is the number of pole-pairs, R is the phase resistance, w is the electrical angular speed, T_e is the electromagnetic torque and L_{dq} are the dq-axis inductances, respectively. Transformation from the rotor frame to the stator flux frame can be obtained from Fig. 1 as follows:

$$\begin{bmatrix} F_f \\ F_\tau \end{bmatrix} = \begin{bmatrix} cos\delta & sin\delta \\ -sin\delta & cos\delta \end{bmatrix} \begin{bmatrix} F_d \\ F_q \end{bmatrix} \quad (4)$$

where F can be any current, voltage or flux linkage vector. δ is known as the torque angle and it is constant in steady-state. From Fig. 1 it can be found that:

$$sin\delta = \frac{\Psi_q}{\Psi_s} \quad \& \quad cos\delta = \frac{\Psi_d}{\Psi_s} \quad (5)$$

where Ψ_s is the magnitude of stator flux linkage vector. Further manipulations of equations (1) - (5) give modelling of IPM-BLAC machines in stator flux frame as follows [4]:

$$\begin{bmatrix} V_f \\ V_\tau \end{bmatrix} = R \begin{bmatrix} I_f \\ I_\tau \end{bmatrix} + \frac{d}{dt} \begin{bmatrix} \Psi_s \\ 0 \end{bmatrix} + \Psi_s \begin{bmatrix} 0 \\ w + \frac{d\delta}{dt} \end{bmatrix} \quad (6)$$

$$T_e = \frac{3p}{2}\left(\frac{\Psi_s \Psi_m \sin\delta}{L_d} + \frac{(L_d - L_q)\Psi_s^2 \sin 2\delta}{2L_d L_q}\right) \quad (7)$$

where $[V_f \quad V_\tau]^T$ and $[I_f \quad I_\tau]^T$ denotes the $f\tau$ frame voltage and current vectors, respectively. Substituting (4) and (5) for the current vector into (3) gives electromagnetic torque as:

$$T_e = \frac{3p}{2}\Psi_s I_\tau \quad (8)$$

B. Current & Voltage Constraints

Equations (9) and (10) give current and voltage constraints of any AC drive. From (9) one can obtain the current limitation as shown in (11). Substituting (11) into (8) yields limitation of electromagnetic torque (12). Considering steady-state and substituting (6) into (10), yields (13). Hence, the stator flux magnitude limit may imposed by (13) in order for a machine to operate in a FW region, too.

$$I_s = \sqrt{I_d^2 + I_q^2} = \sqrt{I_f^2 + I_\tau^2} \le I_{max} \quad (9)$$

$$V_s = \sqrt{V_d^2 + V_q^2} = \sqrt{V_f^2 + V_\tau^2} \le V_{max} \quad (10)$$

$$I_\tau \le \sqrt{{I_{max}}^2 - {I_f}^2} \quad (11)$$

$$T_e \le \frac{3}{2}\, p\, \Psi_s \sqrt{{I_{max}}^2 - {I_f}^2} \quad (12)$$

$$\Psi_s \le \frac{\sqrt{{V_{max}}^2 - (RI_f)^2} - RI_\tau}{w} \quad (13)$$

Current limit in DTC drives is satisfied by limiting torque (12) and FW is achieved by (13).

C. Control Scheme

Fig. 3 illustrates the schematic of the proposed direct torque controlled IPM-BLAC machine drive system, where '*' and '^' denote reference and estimated values, respectively. To achieve MTPA operation the stator flux amplitude is generated by a predefined LUT [19, 24] whose input is electromagnetic torque demand. The flux is limited by (13) for FW operation; hence FW is achieved automatically in DTC drives. The stator flux and torque are controlled by V_f and V_τ voltages, respectively. V_f and V_τ voltages are limited by the over-modulation (OM) block as shown in Fig. 3. The differences between inputs and outputs of the over-modulation block are fed back to the flux and torque PI controllers as anti-windup (AW) to prevent the integrators from winding-up. The coupling term ($w\Psi_s$) in (6) is compensated by the feed-forward as shown in the figure. The reference stator flux amplitude is used in the decoupling as it is clearer than estimated. Feedback (FB) loop is employed as a compensation of the estimated flux in order to prevent late FW triggering of the machine.

Linear torque control conditions can be found in [3, 4, 25]. The maximum torque angle is 90° for non-salient machines (surface mount permanent magnet machines - SPM), 135° for synchronous reluctance machines (SynRM), and $90° < \delta_{max} < 135°$ for salient PM machines where saliency ratio is defined as: $\rho = L_q/L_d$. Low saliency ($\rho \approx 1$) tends to 90° and high saliency tends to 135° for IPM machines [13].

It has been shown that constant switching frequency based DTCs are superior to variable switching frequency based DTCs in many aspects [14, 26]. Hence, space vector pulse width modulation (SVPWM) is increasingly employed in recent drives [27-31]. Therefore, the reference voltages generated in the stator flux frame ($f\tau$) are transformed into the stationary reference frame ($\alpha\beta$) by the inverse Park transformation before being fed to the SVPWM block as shown in Fig. 3.

It is evident that current waveform deteriorates and torque ripple increases in 6 step operation [32-34]. Hence, the voltage is limited in the linear region by the inscribed circle of the hexagon to prevent OM [35].

III. Proposed Flux Observer

The dq-axis observer voltage equations in s-domain are obtained from (1):

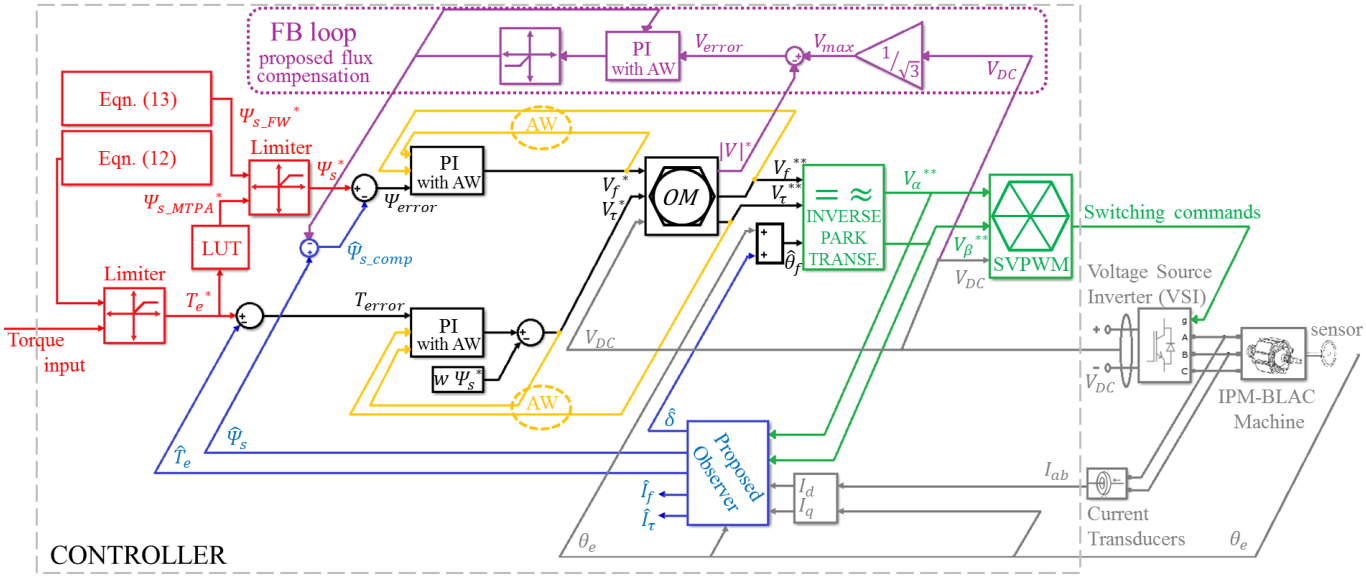

Fig. 3 Proposed DTC scheme of IPM BLAC machine

$$\begin{bmatrix} V_d^{**}(s) \\ V_q^{**}(s) \end{bmatrix} = R_n \begin{bmatrix} I_d(s) \\ I_q(s) \end{bmatrix} + \begin{bmatrix} s & -w \\ w & s \end{bmatrix} \begin{bmatrix} \hat{\Psi}_d(s) \\ \hat{\Psi}_q(s) \end{bmatrix} \quad (14)$$

where ** denotes the inverter reference voltage, ^ denotes the estimated value of the dq-axis flux linkages and R_n is the nominal value of the armature resistance. The dq-axis flux linkages are functions of the dq-axis currents and the rotor position. They are obtained from finite element (FE) analysis of the machine or by experiments.

$$\Psi_d = f(I_d, I_q, \theta_e) \quad \& \quad \Psi_q = g(I_d, I_q, \theta_e) \quad (15)$$

From (15), dq-axis currents can be determined by performing inverses of f and g functions:

$$I_d = f^{-1}(\Psi_d, \Psi_d, \theta_e) \quad \& \quad I_q = g^{-1}(\Psi_d, \Psi_d, \theta_e) \quad (16)$$

High fidelity and computationally efficient, three dimensional (3D) dq-axis flux linkage maps and their inverses which give the dq-axis current maps of a machine, are described in detail in [36, 37]. From the dq-axis current maps of a machine, one can find estimated dq-axis currents from the estimated flux linkages as follows:

$$\hat{I}_d = f^{-1}(\hat{\Psi}_d, \hat{\Psi}_q, \theta_e) \quad \& \quad \hat{I}_q = g^{-1}(\hat{\Psi}_d, \hat{\Psi}_q, \theta_e) \quad (17)$$

Spatial harmonics are accounted in (17) since θ_e variation is included in the inverse functions. 3D $\hat{I}_{dq}$ functions can be converted into 2D by taking the mean value of the rotor angle over one electric period. Thus, f^{-1} and g^{-1} functions in (17) become 2D functions as given in (18) which requires less memory in the observer. By way of example, Fig. 4 (a-b) show the variations of dq-axis current maps versus dq-axis flux linkages, respectively, at 70°C rotor magnet temperature for a 10kW IPM machine designed for EV tractions.

$$\hat{I}_d = f_1(\hat{\Psi}_d, \hat{\Psi}_q) \quad \& \quad \hat{I}_q = g_1(\hat{\Psi}_d, \hat{\Psi}_q) \quad (18)$$

Alternatively, the machine parameters L_d, L_q and Ψ_m are modelled as functions of dq-axis currents. From (2), one obtains the estimated currents as follows:

$$\hat{I}_d = \frac{\hat{\Psi}_d - \Psi_m(I_d, I_q)}{L_d(I_d, I_q)} \quad \& \quad \hat{I}_q = \frac{\hat{\Psi}_q}{L_q(I_d, I_q)} \quad (19)$$

The estimated $\hat{I}_{dq}$ currents in (17) or (18), or nonlinear machine parameters L_d, L_q and Ψ_m are stored in the observer as look-up tables (LUTs). The model predicted currents in any of (17), (18), or (19) are compared with the measured currents and the errors are employed to adjust the input voltages as given in (20).

$$\begin{bmatrix} V_d^{**}(s) \\ V_q^{**}(s) \end{bmatrix} = R_n \begin{bmatrix} I_d(s) \\ I_q(s) \end{bmatrix} + \begin{bmatrix} s & -w \\ w & s \end{bmatrix} \begin{bmatrix} \hat{\Psi}_d(s) \\ \hat{\Psi}_q(s) \end{bmatrix} - \begin{bmatrix} K_p + \frac{K_i}{s} & 0 \\ 0 & K_p + \frac{K_i}{s} \end{bmatrix} \begin{bmatrix} I_d(s) - \hat{I}_d(s) \\ I_q(s) - \hat{I}_q(s) \end{bmatrix} \quad (20)$$

where K_p and K_i are the proportional and integral compensators of the dq-axis flux observers, respectively.

The schematic of the proposed observer is illustrated in Fig. 5. The current errors in the scheme are driven to zero in steady-states. By doing so, the flux estimation errors due to inverter nonlinearities, dead-time and resistance variation with temperature are compensated and the resultant $\hat{\Psi}_{dq}$ will be much close to their actual values.

It should be noted that any forms of (17), (18), or (19) can be employed in the observer. However, (17) and (18) are in general more accurate than the inductances-PM flux representations given in (19) as the cross-coupling effects of dq-axis fluxes are accounted. It should also be noted that (14) cannot estimate the flux linkage in its simple form due to the integrator drift issue. However, the drift will not be present in the proposed observer in Fig. 5 due to the PI compensators.

A. Observer Error Analysis:

For given flux linkages, model dependant dq-axis currents are given by any (17), (18) or (19). However, FE or experimentally derived models in the observer are not perfect due to deviation of the parameters. Any deviation due to material property variation and manufacturing tolerance (e.g. assembly gaps between magnets and the rotor core) can be easily removed by simple calibration based on back-EMF measurements [36, 37]. However, the parameters might deviate depending on the motor temperature. Subtracting (1) from (20) yields;

$$\begin{bmatrix} \Delta V_d(s) \\ \Delta V_q(s) \end{bmatrix} = \Delta R \begin{bmatrix} I_d(s) \\ I_q(s) \end{bmatrix} + \begin{bmatrix} s & -w \\ w & s \end{bmatrix} \begin{bmatrix} \Delta\Psi_d(s) \\ \Delta\Psi_q(s) \end{bmatrix} + \begin{bmatrix} K_p + \frac{K_i}{s} & 0 \\ 0 & K_p + \frac{K_i}{s} \end{bmatrix} \begin{bmatrix} \Delta I_d(s) \\ \Delta I_q(s) \end{bmatrix} \quad (21)$$

where $\Delta V, \Delta R, \Delta\Psi$ and ΔI represent the voltage errors between inverter reference and motor voltages, the resistance error between actual and nominal value, the flux linkage error between actual and estimated fluxes, and the current errors

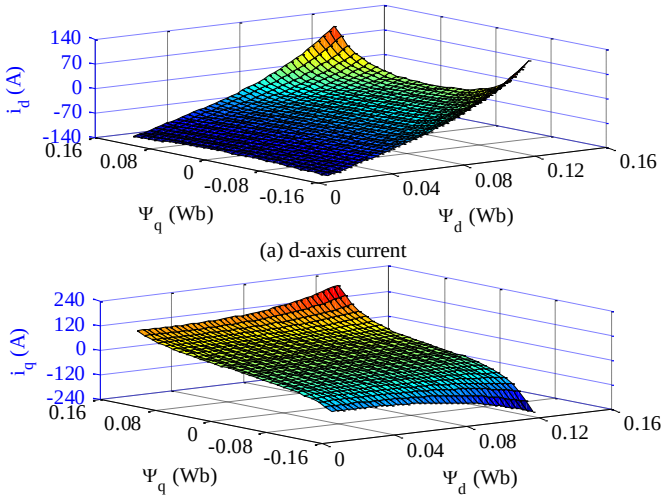

(a) d-axis current

(b) q-axis current

Fig. 4 dq-axis current maps versus dq-axis flux linkages at 70°C rotor temp.

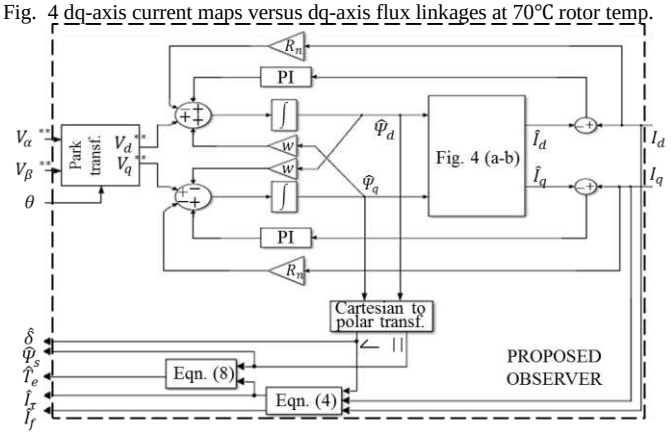

Fig. 5 Proposed observer scheme

This article has been accepted for publication in a future issue of this journal, but has not been fully edited. Content may change prior to final publication. Citation information: DOI 10.1109/TPEL.2016.2524644, IEEE Transactions on Power Electronics

between model predicted and measured currents, respectively. The model predicted currents are obtained from (18):

$$\begin{bmatrix}\hat{I}_d\\ \hat{I}_q\end{bmatrix}=\begin{bmatrix}f_1(\hat{\Psi}_d,\hat{\Psi}_q)\\ g_1(\hat{\Psi}_d,\hat{\Psi}_q)\end{bmatrix}+\begin{bmatrix}\Delta f_1\\ \Delta g_1\end{bmatrix}=\begin{bmatrix}f_1(\Psi_d-\Delta\Psi_d,\Psi_q-\Delta\Psi_q)\\ g_1(\Psi_d-\Delta\Psi_d,\Psi_q-\Delta\Psi_q)\end{bmatrix}+\begin{bmatrix}\Delta f_1\\ \Delta g_1\end{bmatrix} \quad (22)$$

where $[\Delta f_1 \quad \Delta g_1]^T$ are defined as modelling errors. From Taylor's expansion, the above can be expressed as:

$$\begin{bmatrix}\hat{I}_d\\ \hat{I}_q\end{bmatrix}=\begin{bmatrix}f_1(\Psi_d,\Psi_q)+\frac{\partial f_1}{\partial\Psi_d}(-\Delta\Psi_d)+\frac{\partial f_1}{\partial\Psi_q}(-\Delta\Psi_q)\\ g_1(\Psi_d,\Psi_q)+\frac{\partial g_1}{\partial\Psi_d}(-\Delta\Psi_d)+\frac{\partial g_1}{\partial\Psi_q}(-\Delta\Psi_q)\end{bmatrix}+\begin{bmatrix}\Delta f_1\\ \Delta g_1\end{bmatrix} \quad (23)$$

where $f_1(\Psi_d,\Psi_q)=I_d$ and $g_1(\Psi_d,\Psi_q)=I_q$. Hence,

$$\begin{bmatrix}\hat{I}_d\\ \hat{I}_q\end{bmatrix}=\begin{bmatrix}I_d\\ I_q\end{bmatrix}-\begin{bmatrix}J_{11} & J_{12}\\ J_{21} & J_{22}\end{bmatrix}\begin{bmatrix}\Delta\Psi_d\\ \Delta\Psi_q\end{bmatrix}+\begin{bmatrix}\Delta f_1\\ \Delta g_1\end{bmatrix} \quad (24)$$

where $J_{11}=\frac{\partial f_1}{\partial\Psi_d}, J_{12}=\frac{\partial f_1}{\partial\Psi_q}, J_{21}=\frac{\partial g_1}{\partial\Psi_d}, J_{22}=\frac{\partial g_1}{\partial\Psi_q}$.

Therefore, the dq-axis current errors in (21) are given by:

$$\begin{bmatrix}\Delta I_d\\ \Delta I_q\end{bmatrix}=\begin{bmatrix}I_d-\hat{I}_d\\ I_q-\hat{I}_q\end{bmatrix}=\begin{bmatrix}J_{11} & J_{12}\\ J_{21} & J_{22}\end{bmatrix}\begin{bmatrix}\Delta\Psi_d\\ \Delta\Psi_q\end{bmatrix}-\begin{bmatrix}\Delta f_1\\ \Delta g_1\end{bmatrix} \quad (25)$$

Substituting (25) into (21) gives;

$$\begin{bmatrix}\Delta V_d(s)\\ \Delta V_q(s)\end{bmatrix}=\begin{bmatrix}\Delta RI_d(s)\\ \Delta RI_q(s)\end{bmatrix}-\begin{bmatrix}\Delta f_1\left(K_p+\frac{K_i}{s}\right)\\ \Delta g_1\left(K_p+\frac{K_i}{s}\right)\end{bmatrix}+M\begin{bmatrix}\Delta\Psi_d(s)\\ \Delta\Psi_q(s)\end{bmatrix} \quad (26)$$

where $M=\begin{bmatrix}\left(K_p+\frac{K_i}{s}\right)J_{11}+s & \left(K_p+\frac{K_i}{s}\right)J_{12}-w\\ \left(K_p+\frac{K_i}{s}\right)J_{21}+w & \left(K_p+\frac{K_i}{s}\right)J_{22}+s\end{bmatrix}$

The resultant dq-axis flux linkage errors of the proposed observer scheme is obtained from (26) as;

$$\begin{bmatrix}\Delta\Psi_d(s)\\ \Delta\Psi_q(s)\end{bmatrix}=\Delta\Psi_I(s)-\Delta\Psi_R(s)+\Delta\Psi_M(s) \quad (27)$$

where $\Delta\Psi_I, \Delta\Psi_R$ and $\Delta\Psi_M$ are the estimated flux errors due to inverter voltage drop, resistance variation and modelling errors, respectively, and given by (28).

$$\begin{aligned}\Delta\Psi_I(s)&=M^{-1}\begin{bmatrix}\Delta V_d(s)\\ \Delta V_q(s)\end{bmatrix}\\ \Delta\Psi_R(s)&=M^{-1}\begin{bmatrix}\Delta RI_d(s)\\ \Delta RI_q(s)\end{bmatrix}\\ \Delta\Psi_M(s)&=M^{-1}\begin{bmatrix}\Delta f_1\left(K_p+\frac{K_i}{s}\right)\\ \Delta g_1\left(K_p+\frac{K_i}{s}\right)\end{bmatrix}\end{aligned} \quad (28)$$

The steady-state flux linkage errors are obtained by (29).

$$\lim_{s\to0}\begin{bmatrix}\Delta\Psi_d(s)\\ \Delta\Psi_q(s)\end{bmatrix}=\lim_{s\to0}\Delta\Psi_I(s)-\lim_{s\to0}\Delta\Psi_R(s)+\lim_{s\to0}\Delta\Psi_M(s)=\begin{bmatrix}0\\ 0\end{bmatrix}-\begin{bmatrix}0\\ 0\end{bmatrix}+\begin{bmatrix}c_1\\ c_2\end{bmatrix} \quad (29)$$

M^{-1}, c_1, c_2 and detailed theoretical analysis are given in the appendix. c_1 and c_2 are constants associated with the steady-state d- and q-axis flux linkage errors of the proposed observer. (29) theoretically verifies that the proposed observer is independent from inverter voltage drop and resistance variation which are significant issues of conventional schemes. Such inaccuracies are driven to zero at steady states with the proposed observer. However, the last term shows that any modelling error in the observer still exists. In this case, the observer has a filtering effect for reducing measurement noise. The voltage feedback loop in Fig. 3 similar to that in [38] is proposed to compensate for the modelling errors in the field weakening region.

B. Feedback Flux Compensation:

Deviation from the calibrated FE model is dominated by the change in machine operating temperature. A temperature sensor might be utilized to compensate such modelling errors. However, this inevitably adds cost to the system and measured winding temperature might be different from magnet temperature which affects modelling error on flux-linkage.

The temperature effect on the stator flux linkage is investigated with a prototype IPM machine whose specifications are listed in Table I. Table II presents stator flux vector behavior of the machine at different operating temperatures when the torque is 20Nm. It is seen that the increase of the temperature results in decrease in the amplitude and increase in the angle (δ) of the stator flux vector. This can be simply explained by reduction of the magnet flux linkage (Ψ_m) with temperature. Hence, underestimation or overestimation of the flux amplitude occurs when the magnet temperature is lower or higher than the reference temperature (e.g. 70℃ in Fig. 4), respectively. Consequently, the estimated torque angle (δ) will be greater or less than their true value. Because torque is a function of the stator flux vector, the opposite trend of the change of amplitude and torque angle due to temperature results in a less effect on the torque estimation error.

Underestimation of the stator flux amplitude results in the fact that the drive will reach voltage saturation before field weakening is introduced in the stator flux control. The underestimation can be compensated by the voltage feedback loop as illustrated in Fig. 3. When the stator flux is underestimated, the actual flux is greater than the estimation, and hence the amplitude of the control voltage vector will be greater than V_{max} and the voltage error is used by the feedback

TABLE I
SPECIFICATIONS OF PROTOTYPE IPM MACHINE

Number of pole-pairs/Nominal phase resistance	3 / 0.0512 Ω
Continuous current/maximum current	58.5 A / 118 A
DC link voltage	120 V
Base speed / maximum speed	1350/4500 r/min
Continuous torque / peak torque	35.5/70 Nm
Inertia (J)	0.0073 $kg.m^2$
Viscous friction coefficient (B)	1/300 Nm.s/rad
Peak power below base speed	10 kW
Peak power at maximum speed	7 kW

TABLE II
STATOR FLUX VECTOR AT DIFFERENT TEMPERATURES

	Motor magnet temp. (℃)	$\lvert\Psi_s\rvert$ (Wb)	δ (°)
(a)	30	0.1354	30
	60	0.1342	30.8
	100	0.1328	31.8
(b)	30	0.0837	33.9
	60	0.0832	35
	100	0.0821	36.7

(a) $MTPA$ $(w_m=1000\,r/min)$ (b) FW $(w_m=2500\,r/min)$

PI controller to compensate underestimation. Therefore, late triggering of field weakening operation due to flux underestimation can be avoided with the proposed scheme. If the stator flux amplitude is overestimated, the drive will enter the field weakening operation before the voltage limit is reached. However this results in lower estimated torque angle (δ) for a given torque and hence the net effect on torque and drive efficiency is not significant.

IV. Simulation Studies

Several observers will be compared and superiority of the proposed observer will be evidenced by simulation results in this section. To simulate the real electromagnetic behaviour of the IPM machine (Table I), a high-fidelity and computationally efficient machine models [36, 37] at different magnet temperatures are employed in the simulations as given in (16). Inverter nonlinearities are modelled in the simulation with the device data obtained from manufacturer's datasheet. The specifications are listed in Table III. The following observers are employed in the rest of the paper:

- CM_{NOM} represents the current model observer with nominal machine parameters where L_d, L_q and Ψ_m are 0.545mH, 1.571mH and 0.11Wb, respectively.
- CM_{LUT} represents the current model observer with nonlinear machine parameters $L_d(I_d, I_q)$, $L_q(I_d, I_q)$, and $\Psi_m(I_d, I_q)$.
- VM_{LPF} is the voltage model observer where flux is estimated in the stationary frame employing LPFs with required compensations. The cut-off frequency of the filters have been set to 10 Hz.
- HM_{NOM} and HM_{LUT} are the hybrid model observers which combine VM with CM_{NOM} and CM_{LUT}, respectively [5]. The transition speed from CM to VM or vice-versa in HM observers is set to 500 r/min.
- HM_{LUT_LINEAR} is the HM_{LUT} observer with linear flux transition trajectory as shown in Fig. 2-b [8].

Current-flux linkage maps shown in Fig. 4 (a) and (b) at the reference temperature of 70℃ are employed in the proposed observer where the proportional and integral compensators have been set as 6 and 30, respectively.

Fig. 6 illustrates the steady-state errors of the estimated stator flux linkage amplitude and torque which result with the proposed and conventional observers. Observer accuracies are shown as percentages of their actual values defined by $(\text{Estimated}-\text{Actual})/\text{Actual} \times 100$. Motor magnet and winding temperatures were varied but they are assumed to be the same in the simulations for simplicity.

The proposed observer with the proposed FB compensation scheme presents very low estimation errors over wide

TABLE III
Inverter Specifications

T_s - Sampling period	$125\mu s$ (8kHz)
T_d - Dead-time to prevent shoot-through	$3\mu s$
V_{Th}^S - Threshold voltage of active switch	0.85 V
V_{Th}^D - Threshold voltage of freewheeling diode	0.8 V
R_{ON}^S - On-state resistance of active switch	5 mΩ
R_{ON}^D - On-state resistance of freewheeling diode	4.5 mΩ
Manufacturer	Siemens

Torque (Nm)	Motor Temperature °C	Speed 500 a	500 b	1000 a	1000 b	1500 a	1500 b	2500 a	2500 b	3500 a	3500 b	4500 a	4500 b
20	30	1.9	2.5	2.4	2.6	2.1	2.1	1	2.2	0.7	1.8	1.2	1.2
	60	2.8	3.5	2.9	3.1	2.4	2.5	1.4	2.8	1.5	2.7	2.3	2.6
	100	3.8	5	3.5	3.7	2.8	3	2	3.5	2.6	4.2	3.4	4.1
40	30	5	4.8	2.7	3	1.3	1.1	1.7	1.7				
	60	6	6.4	3.4	4	1.9	1.9	2.7	2.8				
	100	7.4	8.5	4.4	5.1	2.7	2.8	4	4.2				
60	30	8.5	8.6	3.2	3.6	1.5	1.1						
	60	9.6	10.3	4.2	5	2.4	2.1						
	100	11.2	13	5.5	7	3.7	3.3						

Outside the operating region

MTPA | FW

(a) Conventional HM_{NOM} observer [5]

Torque (Nm)	Motor Temperature °C	Speed 500 a	500 b	1000 a	1000 b	1500 a	1500 b	2500 a	2500 b	3500 a	3500 b	4500 a	4500 b
20	30	-1.1	-2	-1.1	-2	-1.1	-2	**FB**	-0.5	**FB**	-0.7	**FB**	-1
	60	-0.3	-0.6	-0.3	-0.5	-0.3	-0.6	**FB**	-0.2	**FB**	-0.4	**FB**	-0.5
	100	0.8	1.3	0.8	1.3	0.8	1.3	2.3	0.2	2.9	-0.2	3	-0.2
40	30	-0.4	-1.5	-0.4	-1.5	**FB**	-1.5	**FB**	-0.4				
	60	-0.1	-0.3	-0.1	-0.3	**FB**	-0.5	**FB**	-0.1				
	100	0.3	1.4	0.3	1.4	0.4	0.7	1.1	0.3				
60	30	-0.1	-2	-0.1	-2	**FB**	-1.1						
	60	0	-0.8	0	-0.8	**FB**	-0.5						
	100	-0.1	0.8	0	0.8	0.9	0.3						

Outside the operating region

MTPA | FW

(b) Proposed observer

Fig. 6 Torque-Flux estimation error percentages at steady-states

operating conditions. Torque error at steady state with the proposed scheme is within 2%, whereas the error might increase up to 13% with the HM_{NOM} observer. Similarly, the flux linkage error is within 3% with the proposed observer but it might increase up to 11.2% with the HM_{NOM} observer. Negative signs in the figure indicate that actual value is greater than the reference since estimated value follows the reference in the controller. Thus, any negative flux error indicates late field weakening and positive error causes early field weakening. One can also deduce from the Fig. 6-(a) that there is no negative flux error with the HM_{NOM} observer which proves that the FB loop cannot compensate the steady state errors of the estimated flux since the voltage will not saturate. However, FB in Fig. 6-(b) shows that feedback loop compensates flux errors in FW region when the machine temperature is lower than the reference temperature. It should be noted that any increase in the machine temperature reduces the accuracy of the VM and hence the accuracy of HM based observers since armature resistance increases proportional to temperature of the machine. Fig. 6-(a) shows that its effect on the observer is much more severe than the modelling error of the proposed observer. Simulations with other two hybrid observers, HM_{LUT} and HM_{LUT_LINEAR} have also performed, and the results are similar to that shown in Fig. 6 for HM_{NOM}. It has been found that poor accuracy of the VM based observer interferes with the CM based observer at low speeds, and hence resulting in poor performance of HM type of observers. Further experiments on this effect were performed and the results are presented in section V.

Fig. 7 shows actual torque and flux linkage responses by the VM_{LPF} based observer when the machine operates at 1000 r/min. Ideal inverter has been used until 0.5 second and thereafter nonlinear inverter with dead-time has been represented in the simulations. From the figure, it is seen that

when VM and hence HM (above transition speed) based observer is used, the actual torque and flux of the machine reduce due to inverter voltage drop. It is also important to note that there is an oscillatory response with VM_{LPF} based observer. This is due to presence of the low-pass filters and their magnitude and phase compensations. These problems are not present with the proposed technique whose results are experimentally verified in the next section. It should be noted that the influence of the inverter nonlinearity and voltage drop on the VM based observer in the study is relatively large since the DC link voltage of 120V is quite low.

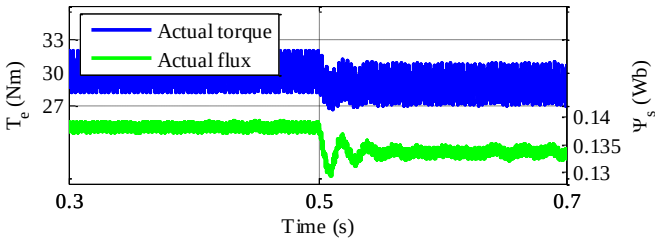

Fig. 7 Inverter nonlinearity effect when VM based observer is employed

V. Experimental Results

In order to validate the performance of the proposed observer both in MTPA and FW regions of a DTC based IPM drive, a test rig with a 10kW IPM-BLAC machine drive designed for traction applications for a wide speed range operation has been established as shown in Fig. 8. The IPM machine, torque transducer and dynamometer are shown in Fig. 8-a, and the controller and inverter are shown in Fig. 8-b. Highly nonlinear machine parameters can be found in [20] and the motor and inverter specifications are provided in Table I and III, respectively. The motor is controlled in torque control mode and the speed is loaded by the dynamometer. The rotor position and the machine torque are measured by a magnetic encoder and a high precision in-line torque transducer, respectively. It should be noted that instantaneous torque cannot be captured due to limited bandwidth, thereby the mean value of the resultant torque is illustrated in the figures. The current waveforms are captured by a power analyzer.

For the purpose of comparison, both the HM_{NOM} based and proposed observers are implemented in the drive and tested. Fig. 9 illustrates the inherent problem of the HM based observers which would exists in recent drives [6, 22, 23]. Because the CM and VM based observers are dominant below and above the transition speed of 500 r/min, respectively, the torque control quality of the drive system with the two observer schemes are compared when the drive speed varies between 300 and 800 r/min. It is seen that, for the reference torque of 20 Nm, 10% torque variation is induced with the HM_{NOM} observer due to the transition from CM to VM modes or vice versa. In contrast, the resultant torque with the proposed observer is robust to speed variation.

Fig. 10 illustrates low speed performance deterioration of the HM based drives. Phase current waveforms of the drive with HM_{LUT}, HM_{LUT_LINEAR} and proposed observers at 100 r/min and 15Nm are presented, respectively. Because of inverter output voltage distortion, the VM based observer accuracy becomes extremely poor at low speeds. Thus, the

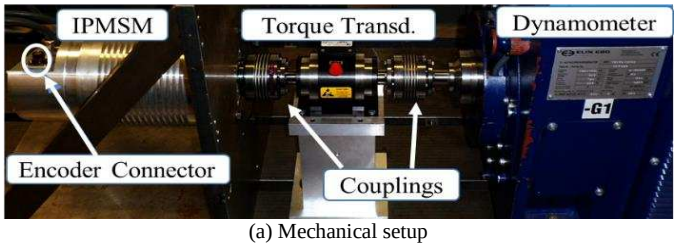

(a) Mechanical setup

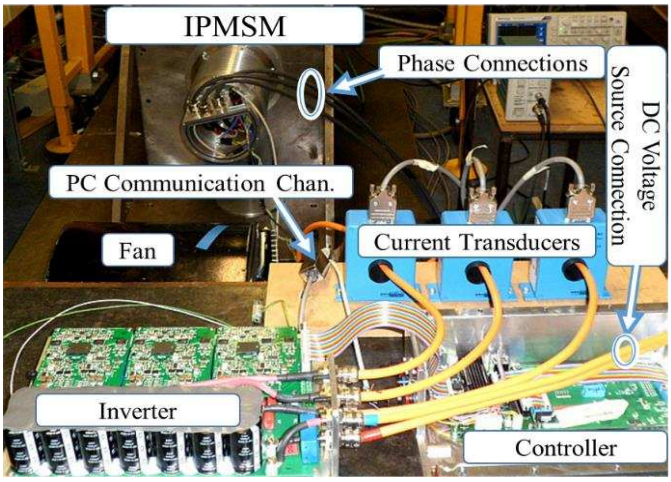

(b) Power electronics converter setup

Fig. 8 View of the experimental hardware setup

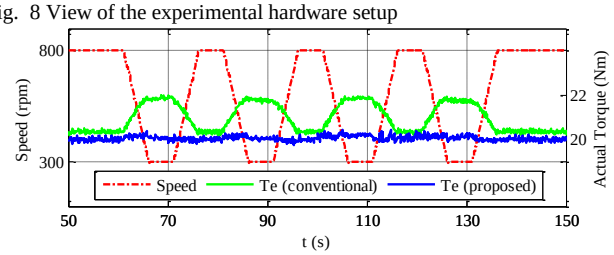

Fig. 9 Transition issue of conventional HM based observers

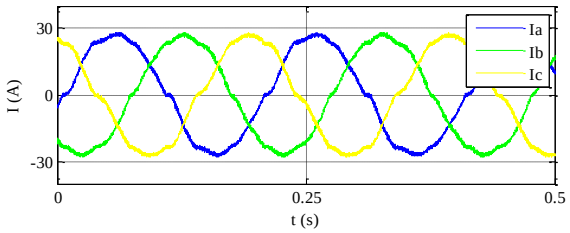

(a) HM_{LUT} observer [5]

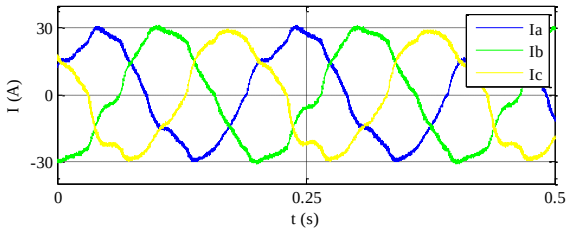

(b) HM_{LUT_LINEAR} observer [8]

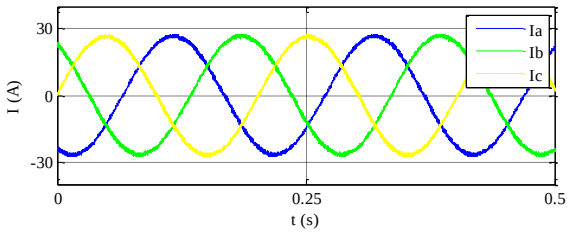

(c) Proposed observer

Fig. 10 Low speed current waveforms 100 r/min 15Nm

HM based observer is affected by the cross-interference issue of the VM part and the performance and current waveforms of the drives deteriorate significantly.

Fig. 11 and Fig. 12 show the current waveforms at 50 and 700 r/min, respectively, with zero torque demand. Phase currents are expected to be very small since the machine operates in MTPA region with zero torque demand. This is, indeed, the case with the proposed observer. However, inaccuracies of the conventional observers cause significant currents to flow even at no load and consequently reducing the drive efficiency. This phenomenon can be understood as follows. Due to torque estimation error the estimated torque tracks the zero torque demand does not mean the actual torque is zero. Hence this is not "no load" operation in strict sense. The amount of current deviation from zero is dependent on the observer error. With the VM based observer, the influence of inverter nonlinearity and voltage drop is still significant even at 700 r/min because of low DC link voltage.

Smooth transitions from MTPA to FW regions of the drive with the proposed observer under no load and 15 Nm torque are given in Fig. 13 (a) and (b), respectively. As will be seen, the flux is automatically weakened in the DTC drives by (13). The results from Fig. 13 to Fig. 16 employ (19), while others employ (18).

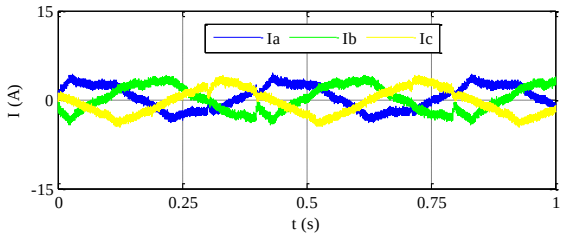

(a) HM_{LUT} observer [5]

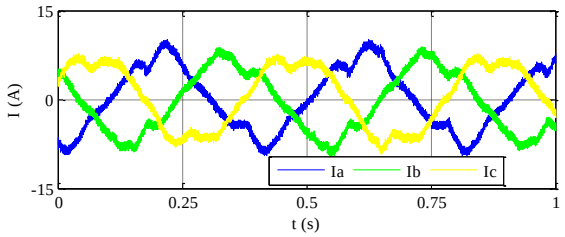

(b) HM_{LUT_LINEAR} observer [8]

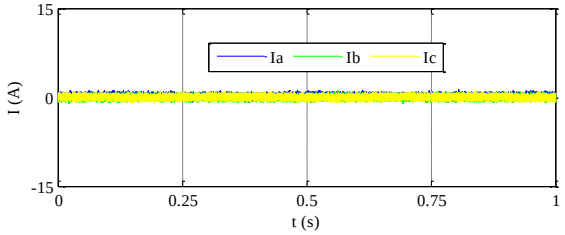

(c) Proposed observer

Fig. 11 Measured current waveforms with zero torque demand at 50 r/min

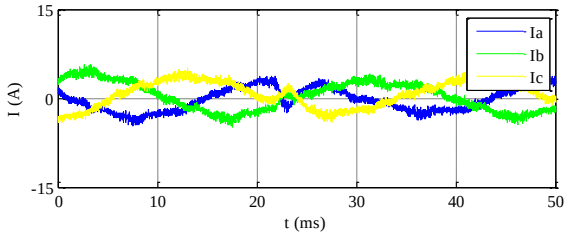

(a) HM_{LUT} observer [5]

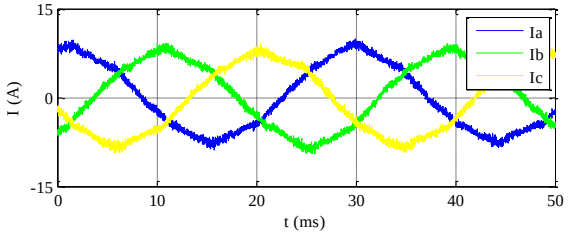

(b) VM_{LPF}

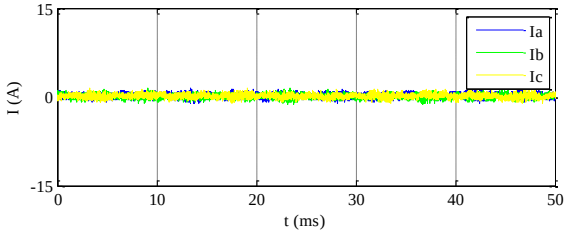

(c) Proposed observer

Fig. 12 Measured current waveforms with zero torque demand at 700 r/min

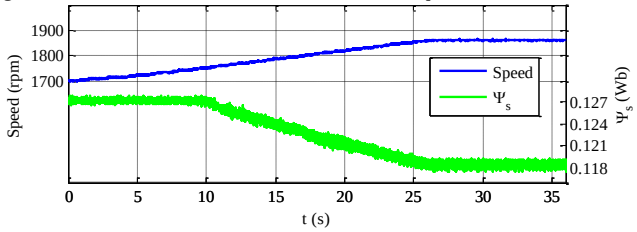

(a) No load transition

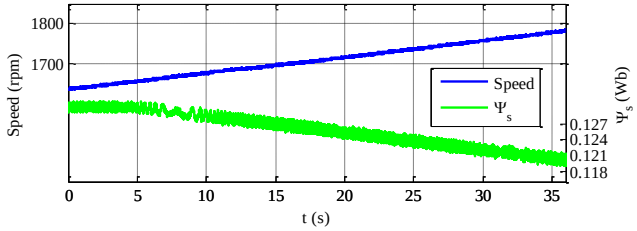

(b) 15 Nm loaded transition

Fig. 13 FW transitions of the drive

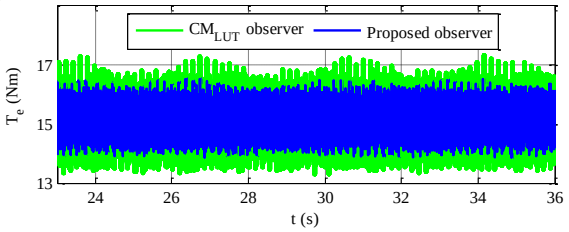

Fig. 14 Torque responses at twice the base speed; 2700 r/min

Fig. 14 shows the estimated torque in steady state at 2700 r/min and 15 Nm when CM_{LUT} and the proposed observers are employed. The proposed observer results in much lower ripple.

Fig. 15 (a) and (b) shows the torque responses of the drive with the proposed observer when the reference torque is increased in a step of 5Nm at 1000 r/min (MTPA) and 2000 r/min (FW), respectively. As can be seen, the actual torque follows closely to the reference which validates the observer accuracy. It should be noted that a rate limiter is imposed on the torque step demand to avoid uncomfortable jerk of the traction system; hence the resultant torque responses are slightly slower.

Fig. 16 (a) illustrates the responses of the estimated torque and flux to a step change in torque demand when the drive

This article has been accepted for publication in a future issue of this journal, but has not been fully edited. Content may change prior to final publication. Citation information: DOI 10.1109/TPEL.2016.2524644, IEEE Transactions on Power Electronics

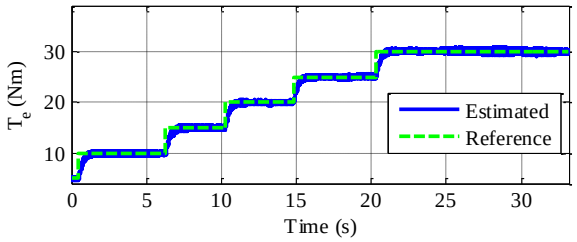

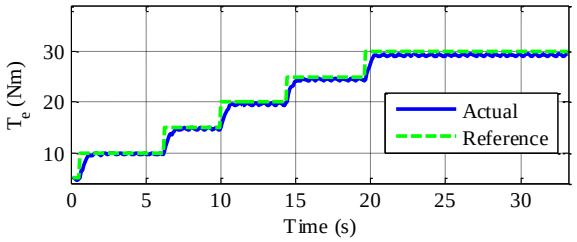

(a) 1000 r/min, MTPA

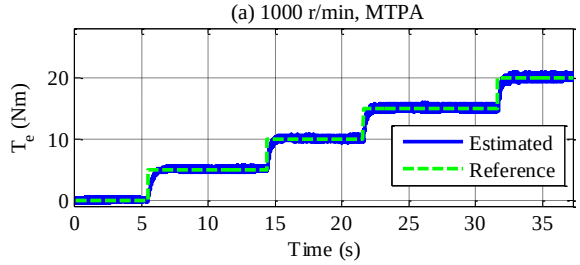

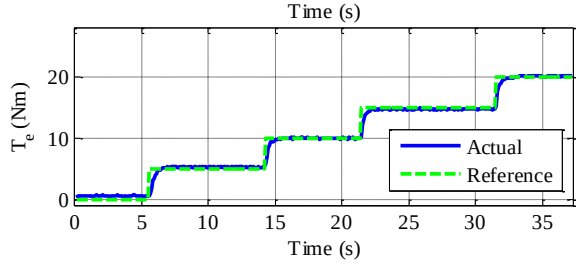

(b) 2000 r/min, FW

Fig. 15 Experimental results of torque step responses with proposed observer

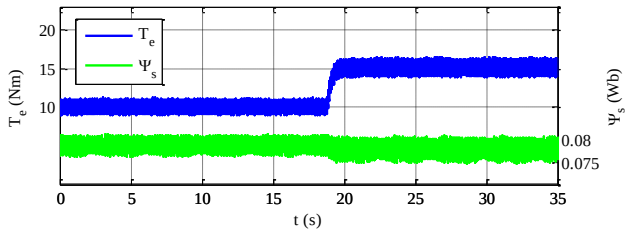

(a) Torque and stator flux responses

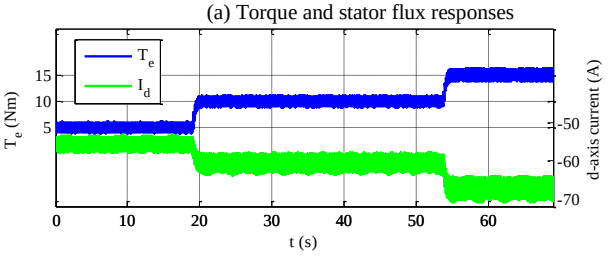

(b) Torque and d-axis current responses

Fig. 16 Drive responses at twice the base speed; 2700 r/min

with the proposed observer operates at 2700 r/min, twice the base speed. A similar response of estimated torque and d-axis current to step changes in torque demands are shown in Fig. 16 (b).

A test in deep FW region has been performed with the proposed observer in order to validate high performance operation and independence of inverter nonlinearities, dead-time and armature resistance variation. The test is performed

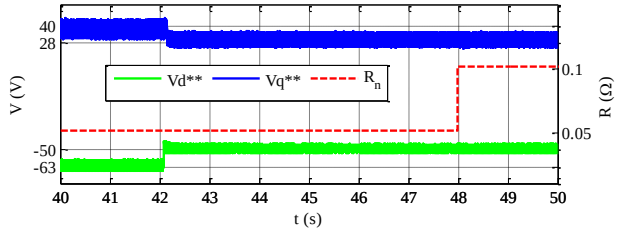

(a) Voltage and resistance disturbances

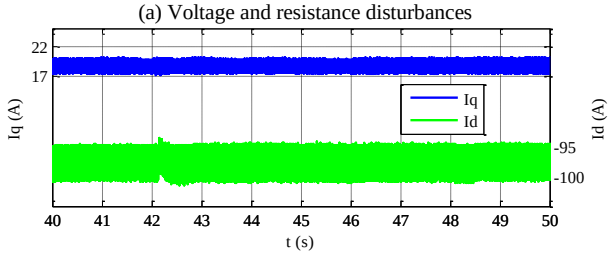

(b) dq-axis currents

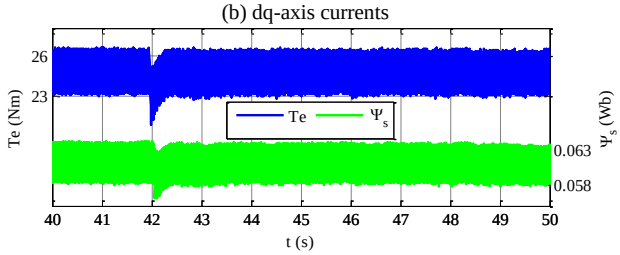

(c) Torque and stator flux responses to disturbances

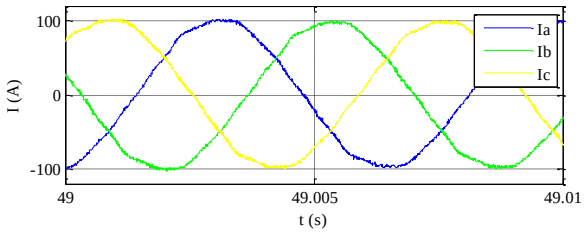

(d) Phase currents after disturbances

Fig. 17 Deep field weakening test at 3000 r/min and 25Nm

at the peak power of 7.85 kW (3000 r/min and 25Nm) and the results are shown in Fig. 17. Disturbances to V_{dq}^{**} and R_n are deliberately injected into the observer shown in Fig. 5 at 42 and 48 seconds, respectively. V_{dq}^{**} and R_n are multiplied by 80% and 200%, respectively. Despite the extremely inaccurate phase voltages and armature resistance information in the observer, the drive is very robust and the disturbances are compensated by measured phase currents via the observer correction mechanism. It is seen from the phase currents that extremely inaccurate phase voltages did not result in deteriorated current waveforms unlike the conventional HM observers. One can deduce the inverter independence by comparing Fig. 7 and Fig. 17 (c).

VI. Conclusions

A novel flux observer for direct torque controlled IPM-BLAC drives has been described in this paper. The observer takes machine nonlinearities into account by high fidelity modelling in order to estimate stator flux and electromagnetic torque of the machine more accurately over a wide speed range. Unlike conventional schemes, it has been proved that the observer is independent from inverter nonlinearities, dead-time, and armature resistance variations since such nonlinearities are compensated by measured phase currents.

Magnetic saturation, cross-coupling effects of flux linkages and spatial harmonics are all considered in the modelling. Additionally, the observer has no filters; hence there is no associated delays and oscillatory responses which are significant concerns of conventional schemes. Low speed performance deterioration associated with conventional observers has also been eliminated by the proposed observer.

It has been shown that the observer is vulnerable to modelling errors which is dominated by machine temperature variation during operation. The modelling error has been partly addressed in the field weakening region by the voltage feedback loop. The influence of the modelling error was investigated by extensive simulations with the high fidelity IPM model. It has been shown that the resultant torque estimation error is relatively small. The superiority and effectiveness of the proposed observer both in transient and steady-states have been verified by extensive simulations and experimental results.

APPENDIX

The elements of the M^{-1} (s) matrix, and the transfer functions associated with $\Delta\Psi_I(s), \Delta\Psi_R(s)$ and $\Delta\Psi_M(s)$ are given by:

$$M^{-1} = \begin{bmatrix} \frac{s^3 + s^2(K_pJ_{22}) + s(K_iJ_{22})}{\sigma_1} & \frac{s^2(w - K_pJ_{12}) - s(K_iJ_{12})}{\sigma_1} \\ -\frac{s^2(w + K_pJ_{21}) + s(K_iJ_{21})}{\sigma_1} & \frac{s^3 + s^2(K_pJ_{11}) + s(K_iJ_{11})}{\sigma_1} \end{bmatrix}$$

where;

$$\boldsymbol{\sigma_1} = \boldsymbol{s^4} + \boldsymbol{s^3}\left(K_p(J_{11} + J_{22})\right) + \boldsymbol{s^2}\left(w^2 + K_i(J_{11} + J_{22}) - wK_p(J_{12} - J_{21}) + {K_p}^2(J_{11}J_{22} - J_{12}J_{21})\right) + \boldsymbol{s}\left(wK_i(J_{21} - J_{12}) + 2K_pK_i(J_{11}J_{22} - J_{12}J_{21})\right) + {K_i}^2(J_{11}J_{22} - J_{12}J_{21})$$

$$\Delta\Psi_I(s) = \begin{bmatrix} \frac{\boldsymbol{s^3}(\Delta V_d(s)) + \boldsymbol{s^2}\left(\Delta V_d(s)K_pJ_{22} + \Delta V_q(s)(w - K_pJ_{12})\right) + \boldsymbol{s}\left(\Delta V_d(s)K_iJ_{22} - \Delta V_q(s)K_iJ_{12}\right)}{\sigma_1} \\ \frac{\boldsymbol{s^3}\left(\Delta V_q(s)\right) + \boldsymbol{s^2}\left(\Delta V_q(s)K_pJ_{11} - \Delta V_d(s)(w + K_pJ_{21})\right) + \boldsymbol{s}\left(\Delta V_q(s)K_iJ_{11} - \Delta V_d(s)K_iJ_{21}\right)}{\sigma_1} \end{bmatrix}$$

$$\Delta\Psi_R(s) = \begin{bmatrix} \frac{\boldsymbol{s^3}(\Delta RI_d(s)) + \boldsymbol{s^2}\left(\Delta RI_d(s)K_pJ_{22} + \Delta RI_q(s)(w - K_pJ_{12})\right) + \boldsymbol{s}\left(\Delta RI_dK_iJ_{22} - \Delta RI_q(s)K_iJ_{12}\right)}{\sigma_1} \\ \frac{\boldsymbol{s^3}\left(\Delta RI_q(s)\right) + \boldsymbol{s^2}\left(\Delta RI_q(s)K_pJ_{11} - \Delta RI_d(s)(w + K_pJ_{21})\right) + \boldsymbol{s}\left(\Delta RI_q(s)K_iJ_{11} - \Delta RI_d(s)K_iJ_{21}\right)}{\sigma_1} \end{bmatrix}$$

$$\Delta\Psi_M(s) = \begin{bmatrix} \frac{\boldsymbol{s^3}(K_p\Delta f_1) + \boldsymbol{s^2}\left(\Delta f_1(K_i + {K_p}^2J_{22}) + \Delta g_1K_p(w - K_pJ_{12})\right) + \boldsymbol{s}\left(2\Delta f_1K_pK_iJ_{22} + \Delta g_1K_i(w - 2K_pJ_{12})\right) + {K_i}^2(\Delta f_1J_{22} - \Delta g_1J_{12})}{\sigma_1} \\ \frac{\boldsymbol{s^3}(K_p\Delta g_1) + \boldsymbol{s^2}\left(\Delta g_1(K_i + {K_p}^2J_{11}) - \Delta f_1K_p(w + K_pJ_{21})\right) + \boldsymbol{s}\left(2\Delta g_1K_pK_iJ_{11} - \Delta f_1K_i(w + 2K_pJ_{21})\right) + {K_i}^2(\Delta g_1J_{11} - \Delta f_1J_{21})}{\sigma_1} \end{bmatrix}$$

It can be shown based on the final value theorem that:

$$\lim_{s\to 0}\Delta\Psi_I(s) = \lim_{s\to 0}\Delta\Psi_R(s) = \begin{bmatrix} \frac{0}{{K_i}^2(J_{11}J_{22} - J_{12}J_{21})} \\ \frac{0}{{K_i}^2(J_{11}J_{22} - J_{12}J_{21})} \end{bmatrix} = \begin{bmatrix} 0 \\ 0 \end{bmatrix}$$

$$\lim_{s\to 0}\Delta\Psi_M(s) = \begin{bmatrix} \frac{{K_i}^2(\Delta f_1J_{22} - \Delta g_1J_{12})}{{K_i}^2(J_{11}J_{22} - J_{12}J_{21})} \\ \frac{{K_i}^2(\Delta g_1J_{11} - \Delta f_1J_{21})}{{K_i}^2(J_{11}J_{22} - J_{12}J_{21})} \end{bmatrix} = \begin{bmatrix} \frac{\Delta f_1J_{22} - \Delta g_1J_{12}}{J_{11}J_{22} - J_{12}J_{21}} \\ \frac{\Delta g_1J_{11} - \Delta f_1J_{21}}{J_{11}J_{22} - J_{12}J_{21}} \end{bmatrix} = \begin{bmatrix} c_1 \\ c_2 \end{bmatrix}$$

REFERENCES

[1] S. Morimoto, Y. Takeda, T. Hirasa, and K. Taniguchi, "Expansion of operating limits for permanent magnet motor by current vector control considering inverter capacity," Industry Applications, IEEE Transactions on, vol. 26, pp. 866-871, 1990.

[2] K. D. Hoang, J. Wang, M. Cyriacks, A. Melkonyan, and K. Kriegel, "Feed-forward torque control of interior permanent magnet brushless AC drive for traction applications," in Electric Machines & Drives Conference (IEMDC), 2013 IEEE International, 2013, pp. 152-159.

[3] K. D. Hoang, Z. Q. Zhu, and M. Foster, "Online optimized stator flux reference approximation for maximum torque per ampere operation of interior permanent magnet machine drive under direct torque control," in Power Electronics, Machines and Drives (PEMD 2012), 6th IET International Conference on, 2012, pp. 1-6.

[4] L. Zhong, M. F. Rahman, W. Y. Hu, and K. W. Lim, "Analysis of direct torque control in permanent magnet synchronous motor drives," Power Electronics, IEEE Transactions on, vol. 12, pp. 528-536, 1997.

[5] P. L. Jansen and R. D. Lorenz, "A physically insightful approach to the design and accuracy assessment of flux observers for field oriented induction machine drives," Industry Applications, IEEE Transactions on, vol. 30, pp. 101-110, 1994.

[6] X. Wei and R. D. Lorenz, "Reduced Parameter Sensitivity Stator Flux Linkage Observer in Deadbeat-Direct Torque and Flux Control for IPMSMs," Industry Applications, IEEE Transactions on, vol. 50, pp. 2626-2636, 2014.

[7] L. Jae Suk, C. Chan-Hee, S. Jul-Ki, and R. D. Lorenz, "Deadbeat-Direct Torque and Flux Control of Interior Permanent Magnet Synchronous Machines With Discrete Time Stator Current and Stator Flux Linkage Observer," Industry Applications, IEEE Transactions on, vol. 47, pp. 1749-1758, 2011.

[8] K. Jang-Hwan, C. Jong-Woo, and S. Seung-Ki, "Novel rotor-flux observer using observer characteristic function in complex vector space for field-oriented induction motor drives," Industry Applications, IEEE Transactions on, vol. 38, pp. 1334-1343, 2002.

[9] Y. Anno and S. Seung-Ki, "Design of Flux Observer Robust to Interior Permanent-Magnet Synchronous Motor Flux Variation," Industry Applications, IEEE Transactions on, vol. 45, pp. 1670-1677, 2009.

[10] Y. Inoue, S. Morimoto, and M. Sanada, "Comparative Study of PMSM Drive Systems Based on Current Control and Direct Torque Control in Flux-Weakening Control Region," Industry Applications, IEEE Transactions on, vol. 48, pp. 2382-2389, 2012.

[11] Y. Inoue, S. Morimoto, and M. Sanada, "Control Method Suitable for Direct-Torque-Control-Based Motor Drive System Satisfying Voltage and Current Limitations," Industry Applications, IEEE Transactions on, vol. 48, pp. 970-976, 2012.

[12] Y. Jeong and S. Sul, "Adaptive Flux Observer with On-line Inductance Estimation of an IPMSM Considering Magnetic Saturation," in Power Electronics Specialists Conference, 2005. PESC '05. IEEE 36th, 2005, pp. 2467-2473.

[13] G. Pellegrino, E. Armando, and P. Guglielmi, "Direct-Flux Vector Control of IPM Motor Drives in the Maximum Torque Per Voltage Speed Range," Industrial Electronics, IEEE Transactions on, vol. 59, pp. 3780-3788, 2012.

[14] T. Lixin, Z. Limin, M. F. Rahman, and H. Yuwen, "A novel direct torque controlled interior permanent magnet synchronous machine drive with low ripple in flux and torque and fixed switching frequency," Power Electronics, IEEE Transactions on, vol. 19, pp. 346-354, 2004.

[15] Y. Inoue, S. Morimoto, and M. Sanada, "Examination and Linearization of Torque Control System for Direct Torque Controlled IPMSM," Industry Applications, IEEE Transactions on, vol. 46, pp. 159-166, 2010.
[16] N. Q. Dai, R. Dutta, and M. F. Rahman, "Comparative performance analysis of field-oriented control and direct torque control for a fractional-slot concentrated winding interior permanent magnet synchronous machine," in Electrical Machines (ICEM), 2012 XXth International Conference on, 2012, pp. 879-885.
[17] M. F. Rahman, M. E. Haque, T. Lixin, and Z. Limin, "Problems associated with the direct torque control of an interior permanent-magnet synchronous motor drive and their remedies," Industrial Electronics, IEEE Transactions on, vol. 51, pp. 799-809, 2004.
[18] G. Pellegrino, R. I. Bojoi, and P. Guglielmi, "Unified Direct-Flux Vector Control for AC Motor Drives," Industry Applications, IEEE Transactions on, vol. 47, pp. 2093-2102, 2011.
[19] Y. Choi, H. Choi, and J. Jung, "Feedback Linearization Direct Torque Control with Reduced Torque and Flux Ripples for IPMSM Drives," Power Electronics, IEEE Transactions on, vol. PP, pp. 1-1, 2015.
[20] T. Sun, J. Wang, and X. Chen, "Maximum Torque per Ampere (MTPA) Control for Interior Permanent Magnet Synchronous Machine Drives Based on Virtual Signal Injection," Power Electronics, IEEE Transactions on, vol. PP, pp. 1-1, 2014.
[21] G. Pellegrino, E. Armando, and P. Guglielmi, "Direct Flux Field-Oriented Control of IPM Drives With Variable DC Link in the Field-Weakening Region," Industry Applications, IEEE Transactions on, vol. 45, pp. 1619-1627, 2009.
[22] G. Pellegrino, B. Boazzo, and T. Jahns, "Plug-in, Direct Flux Vector Control of PM Synchronous Machine Drives," Industry Applications, IEEE Transactions on, vol. PP, pp. 1-1, 2015.
[23] B. Boazzo and G. Pellegrino, "Model Based, Direct Flux Vector Control of Permanent Magnet Synchronous Motor Drives," Industry Applications, IEEE Transactions on, vol. PP, pp. 1-1, 2015.
[24] F. Niu, B. Wang, A. S. Babel, K. Li, and E. G. Strangas, "Comparative Evaluation of Direct Torque Control Strategies for Permanent Magnet Synchronous Machines," Power Electronics, IEEE Transactions on, vol. PP, pp. 1-1, 2015.
[25] M. F. Rahman, L. Zhong, and L. Khiang Wee, "A direct torque-controlled interior permanent magnet synchronous motor drive incorporating field weakening," Industry Applications, IEEE Transactions on, vol. 34, pp. 1246-1253, 1998.
[26] G. Foo and X. Zhang, "A Constant Switching Frequency Based Direct Torque Control of Interior Permanent Magnet Synchronous Motors with Reduced Ripples and Fast Torque Dynamics," Power Electronics, IEEE Transactions on, vol. PP, pp. 1-1, 2015.
[27] X. Zhang and Z. Li, "Sliding Mode Observer-Based Mechanical Parameter Estimation for Permanent-Magnet Synchronous Motor," Power Electronics, IEEE Transactions on, vol. PP, pp. 1-1, 2015.
[28] M. H. Vafaie, B. Mirzaeian Dehkordi, P. Moallem, and A. Kiyoumarsi, "A New Predictive Direct Torque Control Method for Improving Both Steady-State and Transient-State Operations of PMSM," Power Electronics, IEEE Transactions on, vol. PP, pp. 1-1, 2015.
[29] Z. Tang, X. Li, S. Dusmez, and B. Akin, "A New V/f Based Sensorless MTPA Control for IPMSM Drives," Power Electronics, IEEE Transactions on, vol. PP, pp. 1-1, 2015.
[30] F. Mwasilu and J.-W. Jung, "Enhanced Fault-Tolerant Control of Interior PMSMs Based on an Adaptive EKF for EV Traction Applications," Power Electronics, IEEE Transactions on, vol. PP, pp. 1-1, 2015.
[31] M. Gu, S. Ogasawara, and M. Takemoto, "Novel PWM Schemes with Multi SVPWM of Sensorless IPMSM Drives for Reducing Current Ripple," Power Electronics, IEEE Transactions on, vol. PP, pp. 1-1, 2015.
[32] L. Dong-Choon and G. M. Lee, "A novel overmodulation technique for space-vector PWM inverters," Power Electronics, IEEE Transactions on, vol. 13, pp. 1144-1151, 1998.
[33] K. SeHwan and S. Jul-Ki, "Maximum Voltage Utilization of IPMSMs Using Modulating Voltage Scalability for Automotive Applications," Power Electronics, IEEE Transactions on, vol. 28, pp. 5639-5646, 2013.
[34] K. Yong-Cheol, K. Sungmin, and S. Seung-Ki, "Six-Step Operation of PMSM With Instantaneous Current Control," Industry Applications, IEEE Transactions on, vol. 50, pp. 2614-2625, 2014.
[35] R. Ottersten and J. Svensson, "Vector current controlled voltage source converter-deadbeat control and saturation strategies," Power Electronics, IEEE Transactions on, vol. 17, pp. 279-285, 2002.
[36] X. Chen, J. Wang, B. Sen, P. Lazari, and T. Sun, "A High-Fidelity, Computationally Efficient Model for Interior Permanent Magnet Machines Considering the Magnetic Saturation, Spatial Harmonics and Iron Loss Effect," Industrial Electronics, IEEE Transactions on, vol. PP, pp. 1-1, 2015.
[37] X. Chen, J. Wang, and A. Griffo, "A High-Fidelity and Computationally Efficient Electro-thermally Coupled Model for Interior Permanent-Magnet Machines in Electric Vehicle Traction Applications," Transportation Electrification, IEEE Transactions on, vol. PP, pp. 1-1, 2015.
[38] K. Jang-Mok and S. Seung-Ki, "Speed control of interior permanent magnet synchronous motor drive for the flux weakening operation," Industry Applications, IEEE Transactions on, vol. 33, pp. 43-48, 1997.

Mikail Koç (S'15) was born in Turkey. He received the BSc degree from ESOGU University, Eskisehir, Turkey, in 2009 and the MSc degree from Nottingham University, UK, in 2012 both in electrical and electronic engineering. He is currently pursuing the PhD degree in electronic and electrical engineering at the University of Sheffield, UK. His research interests include efficiency optimised control of motors for electric vehicle traction.

Jiabin Wang (S'94–A'96–M'01–SM'03) received the B.Eng. and M.Eng. degrees from Jiangsu University of Science and Technology, Zhenjiang, China, in 1982 and 1986, respectively, and the Ph.D. degree from the University of East London, London, U.K., in 1996, all in electrical and electronic engineering.

Currently, he is a Professor in Electrical Engineering at the University of Sheffield, Sheffield, U.K. From 1986 to 1991, he was with the Department of Electrical Engineering at Jiangsu University of Science and Technology, where he was appointed a Lecturer in 1987 and an Associated Professor in 1990. He was a Postdoctoral Research Associate at the University of Sheffield, Sheffield, U.K., from 1996 to 1997, and a Senior Lecturer at the University of East London from 1998 to 2001. His research interests range from motion control and electromechanical energy conversion to electric drives for applications in automotive, renewable energy, household appliances and aerospace sectors.

He is a fellow of the IET and a senior member of IEEE.

Tianfu Sun (S'15) was born in China. He received B.Eng. degree in mechanical engineering and M.Sc. degree in civil engineering from Dalian University of Technology, Dalian, China, in 2009 and 2012, respectively. He is currently pursuing the Ph.D. degree in electronic and electrical engineering at The University of Sheffield, U.K. His current research interests include electric/hybrid vehicle drives, power-electronic control of electric machines, sensorless drives and optimal control for electric machine.